Bandgap measurement of high refractive index materials by off-axis EELS

Maryam Vatanparast[1], Ricardo Egoavil[2], Turid W. Reenaas[1], Johan Verbeeck[2], Randi Holmestad[1] and Per Erik Vullum[1, 3]

1. *Department of Physics, NTNU (Norwegian University of Science and Technology), 7491 Trondheim, Norway*
2. *EMAT, University of Antwerp, Groenenborgerlaan 171, 2020 Antwerp, Belgium*
3. *SINTEF Materials and Chemistry, 7065 Trondheim, Norway*

Abstract

In the present work Cs aberration corrected and monochromated scanning transmission electron microscopy electron energy loss spectroscopy (STEM-EELS) has been used to explore experimental set-ups that allow bandgaps of high refractive index materials to be determined. Semi-convergence and –collection angles in the μrad range were combined with off-axis or dark field EELS to avoid relativistic losses and guided light modes in the low loss range to contribute to the acquired EEL spectra. Off-axis EELS further supressed the zero loss peak and the tail of the zero loss peak. The bandgap of several GaAs-based materials were successfully determined by simple regression analyses of the background subtracted EEL spectra. The presented set-up does not require that the acceleration voltage is set to below the Čerenkov limit and can be applied over the entire acceleration voltage range of modern TEMs and for a wide range of specimen thicknesses.

Keywords: Low-loss EELS; GaAs; Bandgap measurements; Relativistic losses

1. Introduction

The developments of aberration corrected and monochromated TEMs were expected to revolutionize the access to information about semiconductor bandgaps and optical properties at the nanoscale. Technically, this is the case, scanning transmission electron microscopy (STEM) with a Cs aberration corrected and monochromated electron beam can in combination with electron energy loss spectroscopy (EELS) be used to collect spectroscopy maps that have atomic spatial resolution and an energy resolution that is in the tens of meV range. Even if the spatial resolution of losses in the bandgap regime is limited by inelastic delocalization, the various bandgaps of nanoscale structures can in principle be mapped both easily and quickly. Moreover, since the low-loss region of the EEL spectrum is described classically by the energy-loss function that is determined by the material's dielectric function [1-3], Kramers-Kronig analysis can be used to determine the material's optical response.

However, many semiconductors are also high refractive index materials. The phase velocity of light in the sample material scales with the refractive index, and beam electrons which move faster than this phase velocity of light will suffer from Čerenkov losses (CLs) and Čerenkov photons generated in the low energy range of the loss spectrum [4-5]. Besides the pure relativistic CLs, further low-energy losses appear due to retardation of the beam electrons from surface and interface plasmons (these losses also have relativistic contributions) and from excitation of guided light modes [6]. The probability of generating Čerenkov photons increases with the acceleration voltage (i.e. the speed of the electrons), but disappears below a critical acceleration voltage (Čerenkov limit) determined by the sample's maximum value of the real part of the dielectric function [6]. However, surface and interface plasmon losses and excitation of guided light modes will still be present at acceleration voltages below the Čerenkov limit [6]. For a large and important group of high refractive index materials, such as Ge, Si, GaAs, GaP and many other semiconductors, the Čerenkov limit is below the typical acceleration voltage range of modern TEMs. The Čerenkov limit for GaAs is only 11 keV if the maximum value of the refractive index is used, and 20.6 keV if the refractive index at the bandgap is used [7].

The scattering cross-section for volume losses, including Čerenkov radiation, is further dependent on the thickness of the TEM specimen. If the specimen thickness has a similar magnitude as the wavelength of the emitted Čerenkov photons, the surfaces will damp the CLs. For h-GaN with a Čerenkov limit of 51 keV it has therefore been shown that the correct bandgap at 3.43 eV can be obtained for a specimen thickness up to 0.5 t/λ (λ = the inelastic mean free path) at 200 kV [8]. For GaAs it has been reported that the onset of the Čerenkov radiation is moved to energies above the bandgap if the specimen thickness is below 100 nm at 200 kV [9]. However, later simulations [10] and experimental data obtained with a specimen thickness as low as 0.4 t/λ [1] have shown that relativistic losses and guided light modes contribute with significant signal to the EEL spectrum below the bandgap energy in GaAs.

Another complication is the extremely low signal of the interband transitions compared to the intensity of the zero loss peak (ZLP). Even if the full width half maximum (FWHM) of the ZLP is very low, a careful procedure for handling the tail of the ZLP is important in order to

extract a correct bandgap signal [11]. A vacuum-recorded ZLP is always different from the ZLP in an EEL spectrum acquired from the sample due to phonon and exciton losses, as well as imperfections in the spectrometer, converting elastic scattering which changes the incoming angles into seemingly inelastic signals. Hence, a vacuum-recorded ZLP cannot simply be used to subtract the ZLP and its tail from spectra acquired from the sample. Generally, a fitting procedure for the ZLP, and especially the tail of the ZLP, is preferred. Several methods have been attempted to extract the bandgap by various fitting routines. These routines include the use of a Lorentzian function [12], a seven parameter fit function for ZLP deconvolution [13], a power law background in front of the bandgap [3], and mirroring the left-side tail of the ZLP to the energy loss side [14]. Even if some of these fitting methods can remove phonon and exciton losses in the ZLP tail, relativistic losses present both below and above the bandgap of high refractive index materials cannot reliably be removed by any fitting routine [15].

The bandgap of GaAs has been retrieved in the literature before. In recent work, it has been argued that unwanted spectral contributions can be avoided by working below the Čerenkov limit [1], and that this simplifies credible measurement of bandgap energies. Nevertheless, in the relativistic simulations of valence electron energy-loss spectra of GaAs done by Rolf Erni it was found that the spectra could still be affected by excitation of guided light modes and retardation effects even with electron energies below the Čerenkov limit [10]. These energy losses are represented by a smooth thickness-dependent background, which is difficult to treat when removing the zero-loss peak from the spectra. Attempts to remove this background might be critical for materials with a weak bandgap feature like GaAs and could affect the measured bandgap energy.

CLs and light guided modes are only present at scattering angles below a few tens of μrad [8-10,15]. In normal STEM, the semi-convergence angles of the beam are normally so large [~several mrad] that the convergent beam electron diffraction (CBED) discs have a significant overlap. This also means that the extremely forward scattered CLs, surface losses and guided light modes are still present in the entire diffraction plane. Hence, normal STEM cannot be used to measure the bandgap of high refractive index materials in the standard acceleration voltage range of 60 – 300 kV for most modern TEMs. However, in this work we use a monochromated and probe corrected beam in low-magnification (Low-Mag) STEM mode. In low magnification STEM, semi-convergence and –collection angles in the μrad range are used. Off-axis conditions, i.e. dark field EELS, is further used to suppress the ZLP and to be outside the angular range where CLs and light guided modes hit the spectrometer. Furthermore, the low semi-convergence and -collection angles decrease the detection of phonons (they have a large angular distribution) and interband transitions with a significant momentum transfer. Dark field EELS means that we detect electrons with a momentum transfer. However, because the semi-angles are far down into the μrad range, we can still detect a part of reciprocal space that is close to the centre of the first Brillouin zone (BZ), the Gamma point (Γ), and far from any of the BZ boundaries. Since the valence and conduction bands both are very flat at the BZ centre, the measured bandgap would still be very close to the material's direct bandgap. One of the benefits of the presented methodology is that bandgap of high refractive index materials can be determined at any acceleration voltage and over the entire range of conventional TEM specimen thicknesses. Compared to EELS performed by conventional TEM in diffraction mode, low-mag STEM has important advantages: Most importantly, in Low-Mag STEM a

much higher spatial resolution can be achieved than in conventional TEM mode. The resolution is typically a few nm and dependent on the convergence angle of the beam. Secondly, the camera lengths in conventional TEM mode are not large enough to provide the same small semi-collection angles that can be used in Low-Mag STEM.

After presenting the different experimental set-ups, we will in this paper systematically compare the results from these different methods of band gap measurements of GaAs-based materials.

2. Materials and method

The GaAs-based materials characterized in this work were grown by molecular beam epitaxy (MBE). A high angle annular dark field (HAADF) STEM image of the sample structure is shown in Fig. 1 a). A 400 nm thick $Al_{0.25}Ga_{0.75}As$ layer is grown on top of a (001) GaAs substrate followed by a stack of 20 quantum dot (QD) layers. Each of the QD layers were grown as 2 monolayers thick InAs and they are separated by 20 nm thick $Al_{0.25}Ga_{0.75}N_xAs_{1-x}$ ($x < 0.01$) spacer layers. On top of the QD stack there is a 330 nm thick $Al_{0.25}Ga_{0.75}As$ layer followed by a 50 nm thick GaAs top layer.
Cross-section TEM samples were prepared both by focused ion beam (FIB) and by Ar ion-milling. The FIB samples were prepared by a FEI Helios Nanolab dual-beam FIB equipped with an Oxford Omniprobe. The coarse Ga^+ ion-beam thinning was done at 30 kV acceleration voltage followed by final thinning at 5 kV and 2 kV. A high resolution HAADF STEM image from one of the InAs QD layers is shown in Fig. 1 b) and demonstrates that the samples made purely by FIB have very minor beam damage from the sample preparation. A PIPS II was used to thin the Ar^+ ion-milled samples. Coarse thinning was performed at 3 kV acceleration voltage before progressively reducing the acceleration voltage, finishing at 100 eV. The samples were cooled by liquid N_2 during milling.

The HAADF STEM images in Fig. 1 were taken with a double Cs corrected, coldFEG JEOL ARM 200CF, operated at 200 kV. EELS was performed with a double Cs corrected, monochromated Titan cube, operated at 80 or 120 kV and equipped with a Gatan Imaging Filter (GIF) Quantum ERS spectrometer. An energy dispersion of 0.01 eV/pixel, and a 2.5 mm GIF entrance aperture were used at all times. The GaAs-based material was oriented a few degrees away from the [110] zone axis to avoid strong channeling effects, and to make sure that we are off most Kikuchi bands in the off-axis set-up.

Several set-ups, including both on-axis and off-axis, normal and low magnification STEM mode with the beam on and closely outside (Aloof) the sample, were conducted to find a set-up that would produce credible bandgap measurements.

In normal STEM mode, the semi-convergence and semi-collection angles are both in the milliradian (mrad) range. The simulated convergent beam electron diffraction (CBED) pattern in Fig. 2 a) shows the size of and the distance between the diffraction discs for GaAs along the [110] zone axis, and for a semi-convergence angle of 24.7 mrad at 80 kV. This semi-

convergence angle combined with a 5.8 mrad semi-collection angle (2.5 mm GIF entrance aperture and 2100 mm camera length at 80 kV) give EEL spectra that probe the entire first BZ, in addition to significant parts of second BZ. However, electrons that have received higher momentum transfer will also go onto the spectrometer due the size of the CBED discs. In the Low-Mag STEM set-up the electron beam is much more parallel than in the normal STEM set-up and allows for semi-convergence and semi- collection angles that are both far down into the µrad range. Simulations of the size of and the distance between the diffraction discs for GaAs along the [110] zone axis at 80 kV in the Low-Mag mode are shown in Fig. 2 b). The semi-convergence angle in these simulations is 0.18 mrad and identical to the angle used in our experiments (defined by the 50 µm in diameter condenser aperture). In Fig. 3, the 0.18 mrad semi-convergence angle is combined with our experimental semi-collection angle of 0.11 mrad (2.5 mm GIF entrance aperture combined with a 6100 mm camera length). These semi-angles are now so small that we practically get signal only from the centre of the first Brillouin zone, assuming on-axis conditions. In order to reach off-axis conditions or dark field EELS conditions where the entire 000 diffraction disc falls outside the spectrometer, the diffraction pattern needs to be shifted at least 0.29 mrad (see Fig. 3). However, under such off-axis conditions the region of reciprocal space detected by the spectrometer is still very close to the centre of the 1st BZ. For GaAs along the [110] zone axis, the region of reciprocal space that goes onto the spectrometer is less than 5% away from the Γ point (see Figs. 2 and 3). Since the valence and conduction bands often have parabolic shape at the zone centre, our off-axis conditions should still detect a signal that is very close to the direct bandgap (Fig. 3c)). The relativistic losses, surface modes and bulk waveguide modes are all extremely forward scattered, and exist inside a narrow solid angle that extends out to a few tens of mrad. As such,

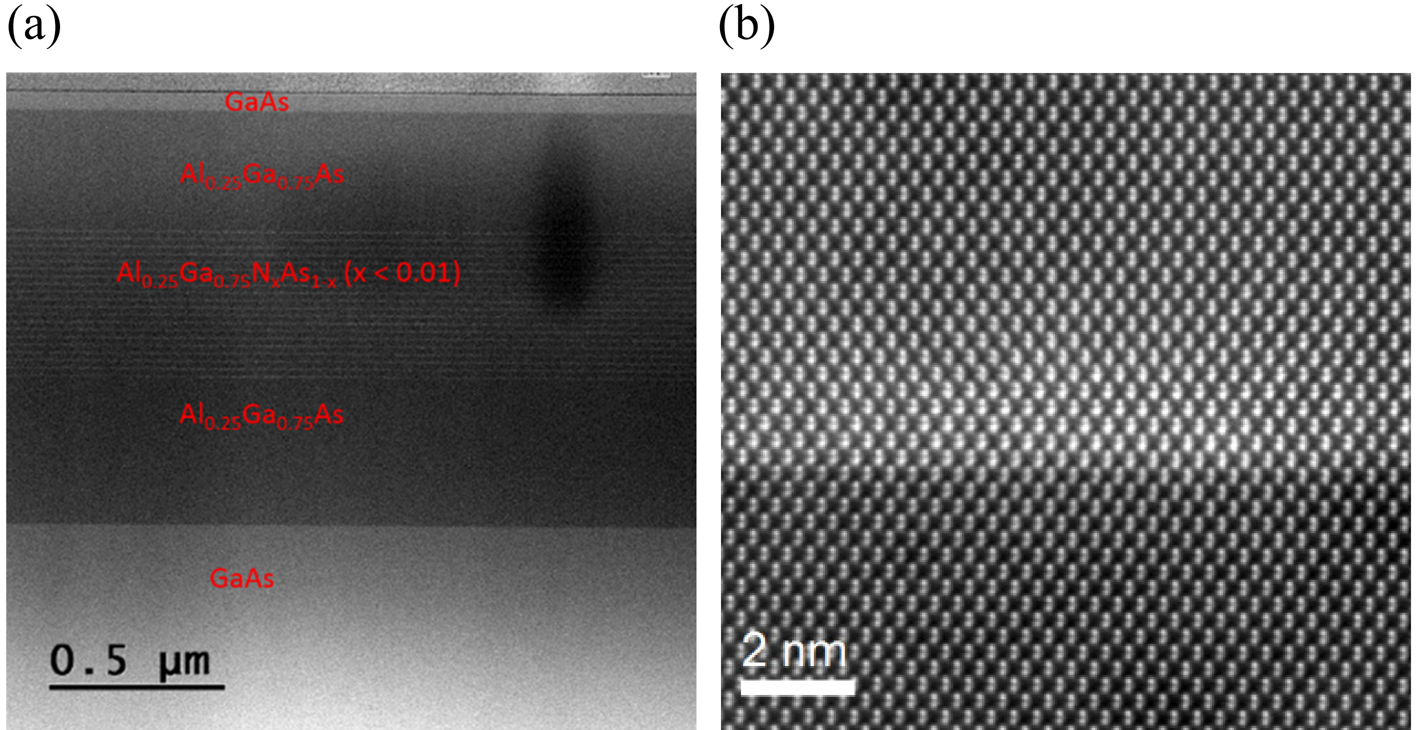

Fig. 1 **(a)** A high angle annular dark field (HAADF) STEM image of the sample structure. A 400 nm thick $Al_{0.25}Ga_{0.75}As$ layer is grown on top of a (001) GaAs substrate followed by a stack of 20 quantum dot (QD) layers. Each of the QD layers were grown as 2 monolayers thick InAs and they are separated by 20 nm thick $Al_{0.25}Ga_{0.75}N_xAs_{1-x}$ ($x < 0.01$) spacer layers. On top of the QD stack there is a 330 nm thick $Al_{0.25}Ga_{0.75}As$ layer followed by a 50 nm thick GaAs top layer. (b) High magnification HAADF-STEM image of an InAs quantum dot from layer 1, In is heavier than Ga, giving higher contrast.

our off-axis conditions are close enough to the centre of the first Brillouin zone to detect bandgap excitations of almost direct bandgap transitions, but still outside the narrow angular range where the unwanted signals from relativistic losses etc. compromise the EEL spectra.

Instead of shifting the 000 diffraction disc outside the spectrometer, another dark field methodology is to acquire two on-axis EEL spectra, but at two different camera lengths. The spectrum taken with the smallest collection angle (largest camera length) is then off-line subtracted from the spectrum taken with the larger collection angle. This difference method has previously been applied to Si [15], but has not been used in the present paper.

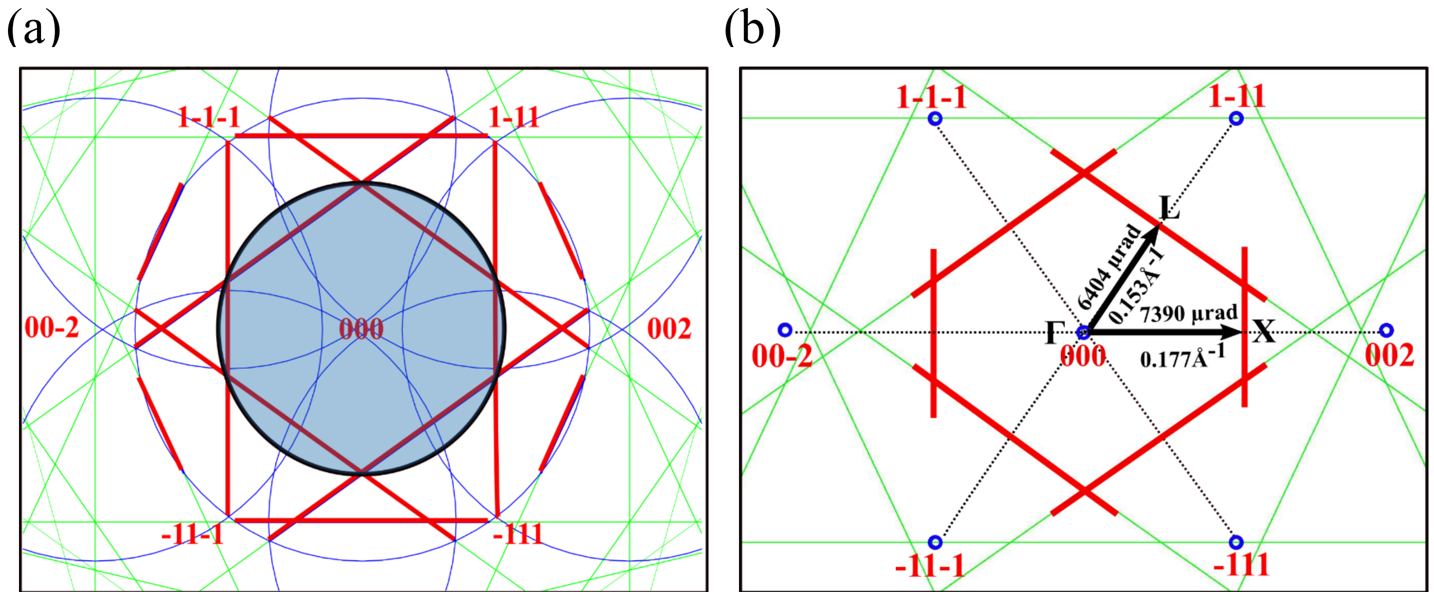

Fig. 2. Simulated CBED patterns from the [011] zone axis orientation in GaAs. (a) and (b) show the size of and the distance between the diffraction discs for GaAs in normal and Low-Mag STEM set-ups, respectively. In the normal STEM mode, a semi-convergence angle of 24.7 mrad combined with a 5.8 mrad semi-collection angle give EEL spectra that probe the entire first BZ, in addition to significant parts of second BZ. In the Low-Mag STEM set-up, the semi-convergence and -collection angles are both far down into the µrad range. The 0.18 mrad semi-convergence angle is combined with a 0.11 mrad semi-collection angle, and we practically get signal from the centre of the first BZ. Green lines are Kikuchi lines, blue circles show the size of CBED disks and the BZ boundaries are shown with red lines. The blue shaded circle shows the semi- collection angle in the normal STEM set-up [24].

Aloof measurements [16] were performed by positioning the beam in vacuum just outside the sample. The idea here was to exploit the long range nature (large impact parameter) of inelastic scattering in the low energy loss regime and simultaneously suppress the unwanted signal in the bandgap region that masks the signal from bandgap excitations. The possible advantage of aloof is that the tail of the ZLP and relativistic losses can be suppressed, although the relative strength of the surface response (e.g. surface plasmons) may be greatly enhanced. To create ideal TEM samples for aloof measurements the final TEM sample was mechanically broken by the tungsten Omniprobe needle in the FIB. This procedure was used to create a TEM sample with a sample facet parallel to the electron beam in order to maximize the interaction between the electron beam and the long-range part of the wave function that describes the sample. Furthermore, this procedure avoids any sample damage caused by the Ar^+ or the Ga^+ ion-beams. In the following result part, EEL spectra from the different set-ups are presented and analysed in order to find the best method for measuring bandgaps in high refractive index materials. Table 1 shows an overview of the different angles used in the different set-ups.

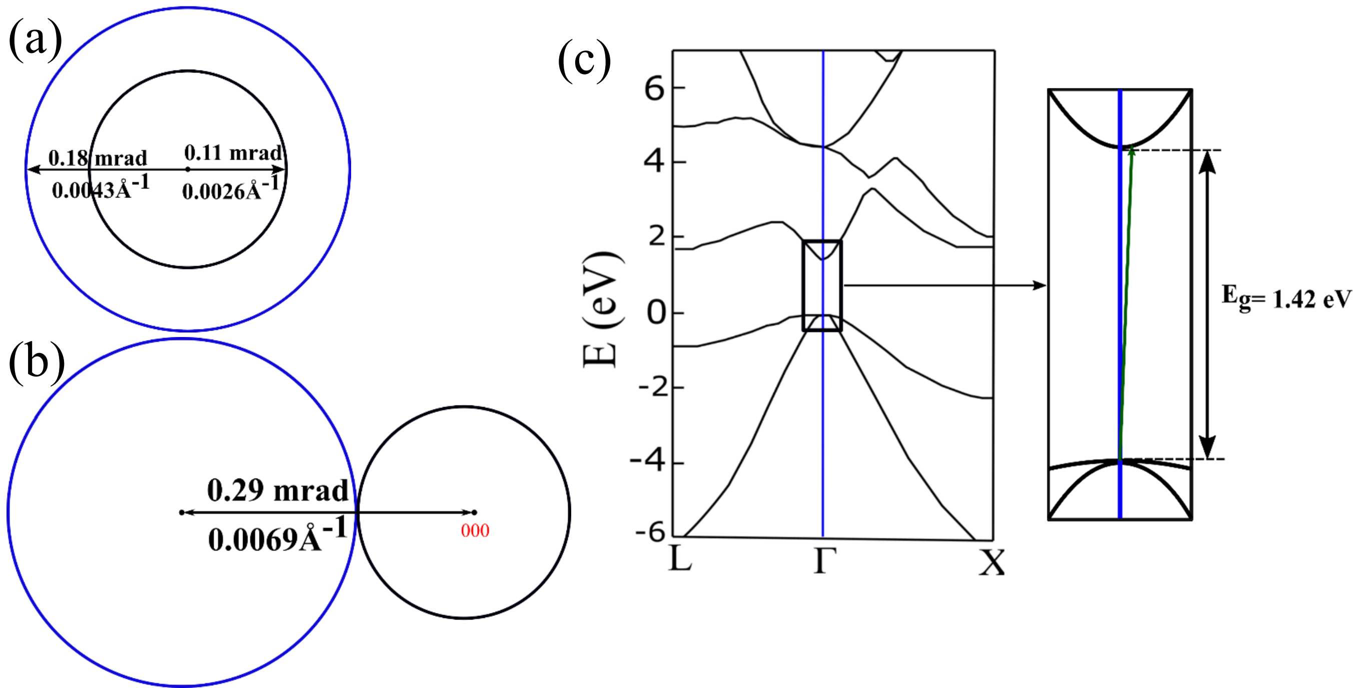

Fig. 3. The 0.18 mrad semi-convergence angle (blue circle) combined with a 0.11 mrad semi-collection angle (black circle) in Low-Mag on-axis (a) and Low-Mag off-axis (b) set-ups are illustrated. In off-axis or dark field EELS conditions the entire 000 diffraction disc falls outside the spectrometer, when the diffraction pattern is shifted more than 0.29 mrad. Under such off-axis conditions the region of the reciprocal space detected by the spectrometer is still very close to the centre of the 1st BZ. For GaAs along the [110] zone axis, the region of reciprocal space that goes onto the spectrometer is less than 5% away from the Gamma point. The band diagram for GaAs is shown in (c). The marked rectangle is magnified to the right. The green arrow represents the experimental condition in (b) where we measure the bandgap 0.0069$Å^{-1}$ from on-axis conditions. We see that the measured indirect bandgap is very close to the direct one.

Table 1. Semi-convergence and -collection angles used in the different set-ups tested in this work.

	Acceleration voltage (kV)	Semi-convergence angle (mrad/Å^{-1})	Semi-collection angle (mrad/Å^{-1})
Normal STEM set-up (Fig. 1)	**200**	**27.7/1.10**	**-**
Normal STEM set-up (Fig. 5)	**120**	**24.7/0.737**	**64.7/1.93**
Normal STEM set-up (Figs. 2a, 4a, 4b and 8)	**80**	**24.7/0.591**	**5.8/0.139**
Low-Mag STEM set-up (Fig. 6)	**80**	**0.11/0.0026**	**0.11/0.0026**
Low-Mag STEM set-up (Figs. 2b and 7)	**80**	**0.18/ 0.0043**	**0.11/0.0026**

3. Results and discussion

3.1. Normal STEM on-axis

We first tried to duplicate earlier obtained results for the bandgap in GaAs [1,6] by using normal STEM mode. Measurements were performed at 80 and 120 kV and variable TEM specimen thicknesses. Furthermore, dual EELS mode was used to maximize the signal to noise in the energy loss region of the bandgap, as the intense part of the ZLP was positioned outside the spectrometer in the "high loss" spectrum. Independent of TEM sample thickness and acceleration voltage, no distinct feature due to bandgap excitations can directly be observed in any of the raw spectra. One such spectrum, acquired at 80 kV and at a sample thickness of 0.75 λ (λ is the inelastic mean free path at 80 kV) is shown in Fig. 4 a). An increased intensity with onset of distinct features just below 3 eV and at 5 eV is expected and fits well with calculated loss spectra of GaAs [6, 10]. Several background subtraction methods were approached in order to reliably subtract the tail of the ZLP. However, methods such as mirroring the left side (negative energy losses) of the zero loss to the right side (positive energy losses), or to use the ZLP acquired in vacuum to subtract the background, both failed. The reason these methods fail can clearly be seen in Fig. 5 where an EEL spectrum acquired in vacuum is compared with the spectrum acquired under the same conditions on the GaAs-based structure. It is not only the tail of the ZLP in the loss region before the bandgap energy that changes significantly, but even the full width at half maximum (FWHM) of the ZLP changes from 0.10 eV in vacuum to 0.14 eV on the sample. A large semi-collection angle of 64.7 mrad was used during the acquisition of the spectra in Fig. 5. Hence, phonon and multi-phonon excitations contribute strongly to the spectrum, in addition to other significant losses such as intraband transitions, relativistic losses, guided light modes and surface and interface related losses in the pre-bandgap region.

Furthermore, the relative strength of most of these losses, which masks the signal from bandgap excitations, is dependent on the sample's chemical composition, sample thickness and crystal orientation as well as acceleration voltage and semi-convergence and –collection angles.

The EEL signals in Fig. 4 b) were produced with a standard "power law" background subtraction model. A power law function gives a very good fit to the spectrum in the entire range from ca. 1.0 – 2.5 eV loss if the width of the energy window chosen to fit the power law function is chosen wisely. However, such an approach can give a bandgap that can take any value in the range 1.0 – 2.5, including the known direct bandgap of GaAs at 1.42 eV.

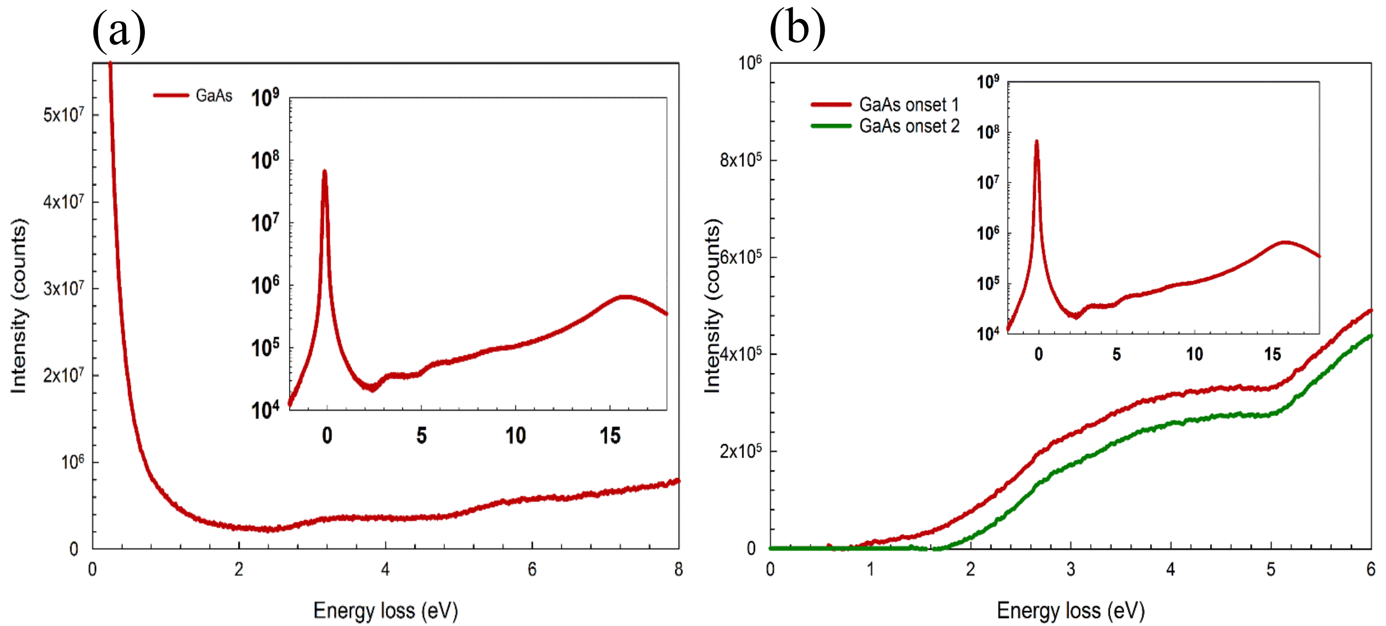

Fig. 4. (a) Raw EELS spectrum acquired from the normal STEM set-up at 80kV. No distinct feature due to bandgap excitations can be directly observed in any of the raw spectra. (b) Different bandgap onsets for GaAs in the normal STEM set-up after background subtraction. The EEL signals produced with a standard "power law" background subtraction model. A power law function gives a very good fit to the spectrum in the entire range from ca. 1.0 – 2.5 eV loss if the width of the energy window chosen to fit the power law function is chosen wisely. This approach can reproduce a bandgap that can take any value in the range between 1.0 – 2.5 eV, including the known direct bandgap of GaAs at 1.42 eV. The entire EEL spectrum is shown in the inset.

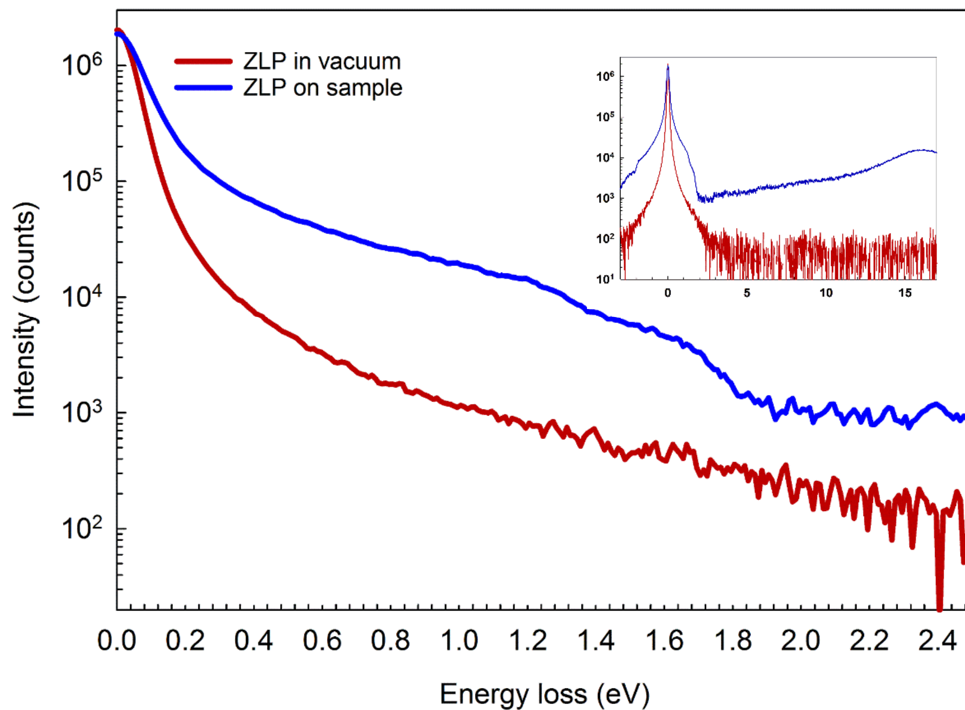

Fig. 5. An EEL spectrum acquired in vacuum is compared with the spectrum acquired under the same conditions on the GaAs-based structure. The tail of the ZLP in the loss region before the bandgap energy changes significantly, and the full width at half maximum (FWHM) of the ZLP changes from 0.10 eV in vacuum to 0.14 eV on the sample. A large semi-collection angle of ca. 64.7 mrad was used during the acquisition of the spectra. The entire EEL spectra are shown in the inset. All spectra are shown in logarithmic scale. The spectrum was acquired at 120 kV and at a sample thickness of 0.55 λ.

3.2. Low-Mag on-axis

In Low-Mag STEM mode, the semi-convergence and –collection angles are both very small, as illustrated in Figs. 2 and 3. The region of reciprocal space collected by the spectrometer is now confined to a narrow circle with a radius of 0.11 mrad only. For GaAs, as well as most other practical samples, this region is far from the first BZ boundaries. GaAs oriented close to the [110] zone axis has its X and L points at the BZ boundary along the [002] and [111] directions located 7.39 and 6.40 mrad away from the BZ centre, respectively. Hence, only the centre of the BZ goes onto the spectrometer. This means that any inelastic transitions with a

significant momentum transfer, such as the major part of all phonons and intraband excitations and a significant part of all surface and interface plasmons, do not contribute to the EEL spectrum. An on-axis EEL spectrum from GaAs, acquired at 80 kV and at a sample thickness of 0.75 λ, and with semi-convergence and –collection angles both equal to 0.11 mrad, is shown in Fig. 6. Despite the suppression of a lot of the signal that masks and buries the signal from bandgap excitations, no sign of any optical onset from a direct bandgap at 1.42 eV can be observed directly in the unprocessed spectrum. Attempts to remove the background end up similar to the case where larger semi-angles are used and give a background subtracted signal with an onset energy anywhere between 1 and 2.5 eV, depending on the background subtracted. Obviously, relativistic losses and guided light modes still dominate the intensity in the energy loss region of the bandgap.

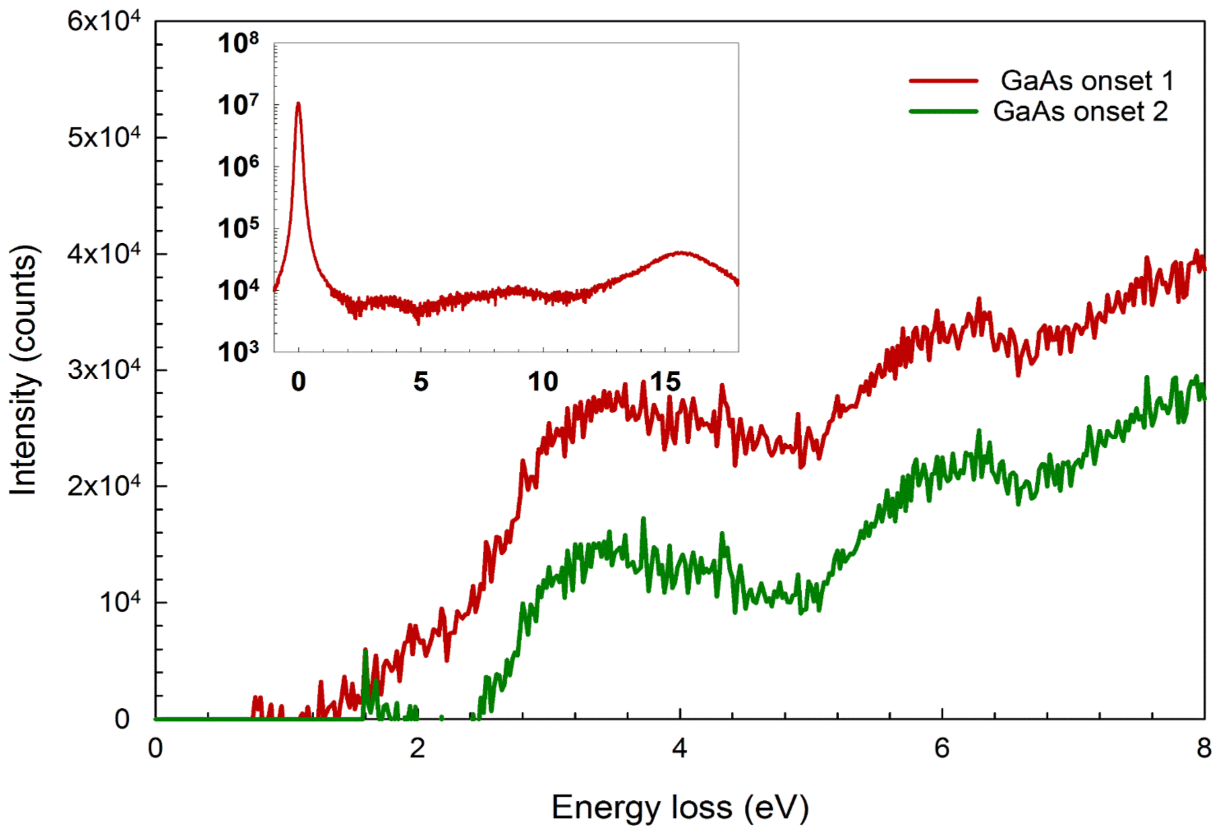

Fig. 6. Different bandgap onsets for GaAs in the Low-Mag STEM set-up after background subtraction. Low-Mag on-axis EEL spectrum from GaAs, acquired at 80 kV and with semi-convergence and –collection angles both equal to 0.11 mrad. No sign of any optical onset from a direct bandgap at 1.42 eV can be observed directly in the unprocessed spectrum. Attempts to remove the background end up similar to the case where larger semi-angles are used and give a background subtracted signal with an onset energy anywhere between 1 and 2.5 eV, depending on the background subtracted. The entire EEL spectrum in logarithm scale is shown in the inset.

3.3. Low-Mag off-axis:

The semi-convergence and collection angles in Low-Mag STEM mode are almost two orders of magnitude less than the angle between the BZ centre and the first BZ boundary. The EEL spectra shown in Fig. 7 are acquired at 80 kV and at a sample thickness of 1.5 λ by using the projector lenses to shift the diffraction plane and move the entire 000 diffraction disc outside the spectrometer. This shift is just larger than 0.29 mrad to overcome the sum of the experimental semi-convergence and –collection angles of 0.18 and 0.11 mrad respectively (see Fig. 3 b)). Firstly, this off-axis shift is so small that the spectrum is collected from a region very close to the centre of the BZ, and hence contains excitations with very small momentum transfer and that are close to direct bandgap excitations. Secondly, this off-axis shift is still large enough to avoid the forward scattered relativistic losses and guided light modes to contribute to the spectrum. Spectra from GaAs, $Al_{0.25}Ga_{0.75}As$ and $Al_{0.25}Ga_{0.75}As_{1-x}N_x$ ($x \ll 1$) are shown in Fig. 7. The three spectra are background subtracted by a power law function in the region 0.5 – 1.2 eV. Least square fitting has further been used to fit the background subtracted spectra below 2.75 eV, and the corresponding regression lines are added in Fig. 7. The onset of bandgap excitations is defined to where the regression line crosses zero intensity. Bandgap values are 1.32 eV ± 0.04 (GaAs), 1.55 eV ± 0.06 eV ($Al_{0.25}Ga_{0.75}As_{1-x}N_x$) and 1.70 eV ± 0.03 ($Al_{0.25}Ga_{0.75}As$), and where the inaccuracies are the width of the 95 % confidence interval associated with each of the regression curves from the least square fitting. These bandgap values are close to the known (1.42 eV for GaAs and 1.77 eV for $Al_{0.25}Ga_{0.75}As$) or expected (ca. 1.65 eV for $Al_{0.25}Ga_{0.75}As_{1-x}N_x$) direct bandgaps for these materials [17-19]. Various background subtraction windows inside the region 0.5 – 1.2 eV gave only insignificant variations in the energy-onset of the bandgap signal. The extracted bandgaps were further determined at several locations along the line scans. Variations in the measured inelastic onset energies were ± 0.05 eV inside regions that were expected to be homogenous. Generally, we observe bandgaps that are about 0.1 eV less than the known or expected bandgap values. This disagreement between the observed onset of inelastic scattering and the onset of the optical bandgap is likely related to the relatively poor energy resolution of the off-axis set-up. The long exposure time of a few seconds reduced the energy resolution (FWHM) to 0.25 eV (due to energy oscillations of the spectrum with a higher frequency than the spectrum acquisition time) that smears the signal to both lower and higher energies. We also notice that the background subtracted spectra in Fig. 7 show a linear signal above the bandgap energy, compared to the $(E - E_g)^{½}$ curvature that is expected for direct bandgap materials [20]. This deviation in the expected shape of the signal can be explained by the fact that we do not probe the entire 1st BZ, but only a small fraction of the 1st BZ, as described in Fig. 3 b). As a consequence of the off-axis set-up we do not collect all excitations to the conduction band, and hence only a limited fraction of the joint density of states (JDOS) is probed. As such, our signal should not be proportional to the entire JDOS, that scale with $(E - E_g)^{½}$, but only to the states determined by the GIF entrance aperture.

The off-axis shift of the CBED pattern giving dark field EEL conditions has several implications: The ZLP peak is strongly suppressed, and in our experimental spectra, the maximum intensity of the ZLP has the same order of magnitude as the maximum intensity of the first bulk plasmon peak at about 15 eV (see inset in Fig.7). Whether or not we are on or off one or several of the major Kikuchi bands would strongly determine how much the ZLP is

damped. The spectra in Fig. 7 were acquired without any knowledge of the position of the Kikuchi bands relative to the region in reciprocal space that was probed. However, this is likely to be an important experimental parameter if it is very important to damp the ZLP as much as possible, for instance if bandgaps in the region below 1 eV are to be determined.

Off-axis conditions combined with very small convergence and collection angles further cause the overall EEL signal to decrease by orders of magnitude compared to on-axis conditions in normal STEM mode where semi-convergence and –collection angles are tens of mrad. To test the robustness of the measurements above, the monochromator slit was therefore changed from 1 to 2 μm in diameter and the condenser aperture was changed from 30 to 50 μm in diameter to increase the probe current from 50 to 400 pA. The change to a larger slit means that we decrease the EEL energy resolution, and the change of condenser aperture size causes the semi-convergence angle to increase from 0.11 to 0.18 mrad. The spatial resolution in the STEM image however, is not reduced rather improved by the change to a larger condenser aperture since the spatial resolution is no longer limited by the lens aberrations in Low-Mag mode due to the very low beam convergence angle. In addition, the acquisition time was set to a few seconds for each pixel in the line scans and maps to have sufficient signal to noise ratios. The larger monochromator slit size combined with acquisition times of several seconds increased the FWHM to 0.2 - 0.3 eV. However and as can be seen in Fig. 7, the tail of the ZLP has totally decayed below 1 eV, and the unprocessed spectra have a nearly flat background signal for several hundred meV in front of the onset of the bandgap for GaAs.

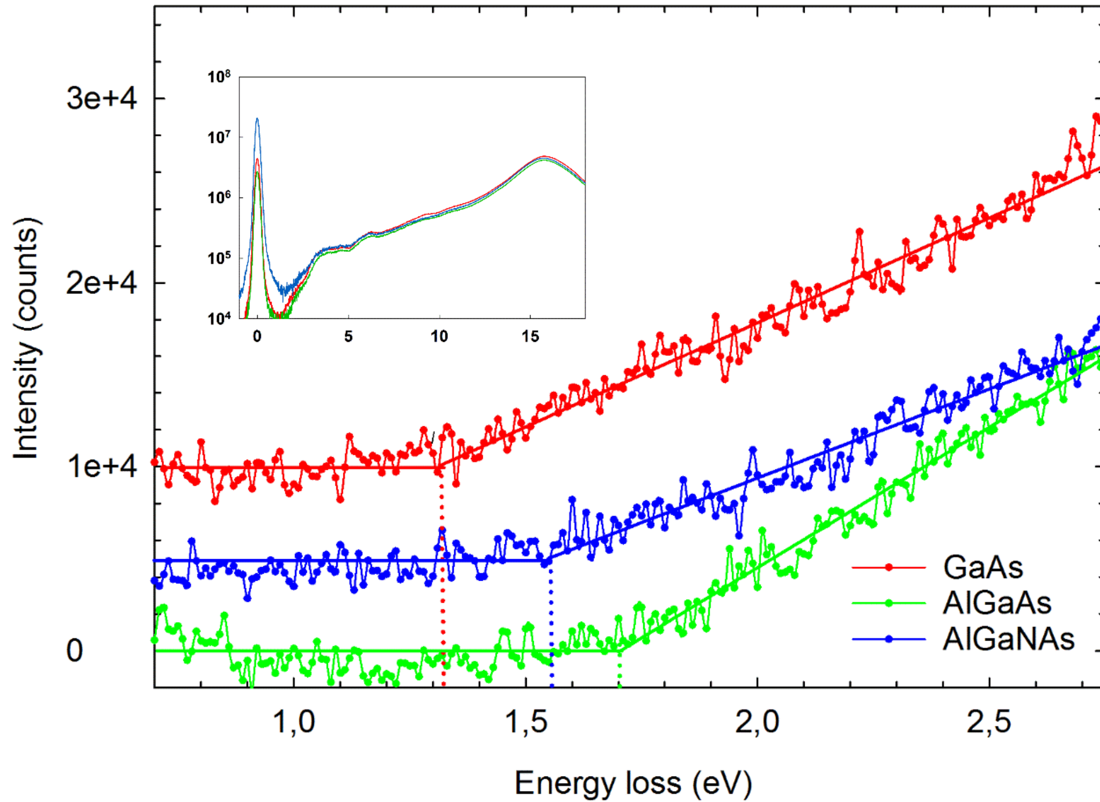

Fig. 7. Background subtracted spectra from GaAs, $Al_{0.25}Ga_{0.75}As$ and $Al_{0.25}Ga_{0.75}As_{1-x}N_x$ ($x < 1$) acquired in the Low-Mag off-axis set-up as shown in Fig. 3b). These spectra are taken from a single line scan that goes from vacuum and through the various layers and ends in the GaAs substrate. Each of the spectra are from the central part of the GaAs, AlGaAs and AlGaNAs layers to avoid any contribution from the nearby layers or from interfaces. The spectra from AlGaNAs and GaAs are shifted vertically by 5000 and 10000 counts for clarification. The bandgap is defined as where the regression lines from the least square fitting cross zero intensity (represented by the horizontal lines). The significant decrease of the ZLP under off-axis conditions is shown in the unprocessed EEL spectra in the inset.

3.4. Aloof:

The long-range Coulomb interactions between the fast electrons in the electron beam and the sample electrons that define a scattering centre, give a large delocalisation effect, which is utilized in the aloof technique. An electron beam that is positioned several nm away from the sample can still excite inelastic transitions in the sample due to this delocalization [21-23]. It has been shown that for instance bandgaps and surface plasmons can be excited and detected several tens of nm nanometers away from the sample. Furthermore, when the beam never goes through the sample one would expect to suppress the relativistic losses and guided light modes in the spectra. Line scans both parallel, at distances from 2 nm to tens of nm, and perpendicular to the sample were acquired to try to retrieve the onset of the bandgap in the nearby sample

material. However, and independent of the distance from the sample, we were not able to observe any bandgap signal in the spectra. An on-axis spectrum collected 30 nm away from the broken edge of GaAs and taken with semi-convergence and –collection angles of 24.7 and 5.8 mrad, respectively, at 80 kV is shown in Fig. 8. Even if the tail of the ZLP is strongly suppressed compared to a similar spectrum acquired on the sample, no bandgap signal could be retrieved from the spectrum, so that any kind of screening effect in GaAs-based materials could be the reason.

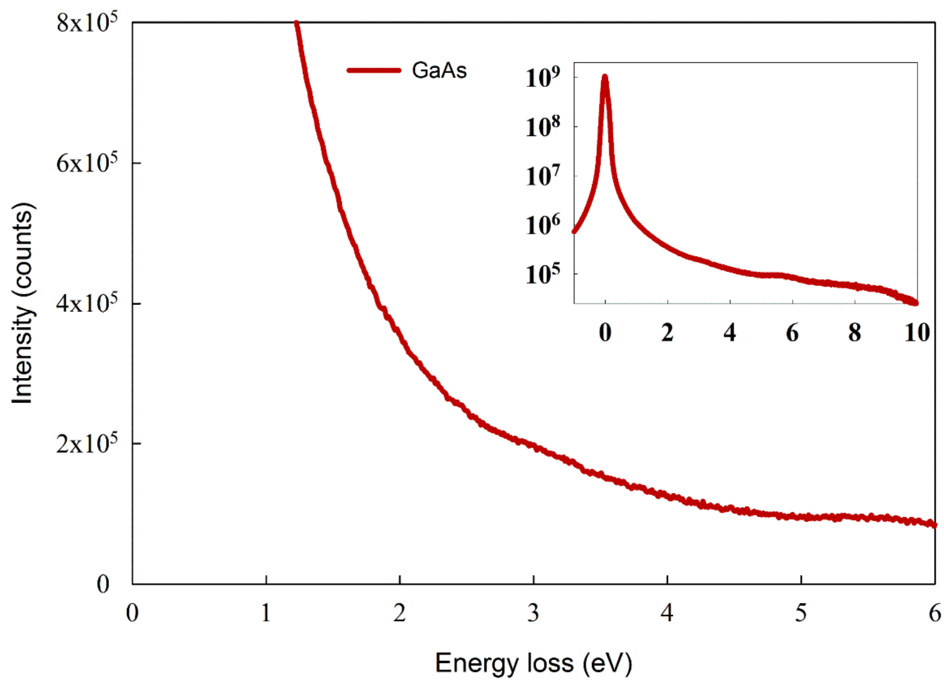

Fig. 8. The on-axis spectrum in the Aloof set-up collected 30 nm away from the broken edge of GaAs and taken with semi-convergence and –collection angles of 27.4 and 5.8 mrad at 80 kV. Even if the tail of the ZLP is strongly suppressed compared to a similar spectrum acquired on the sample, no bandgap signal could be retrieved from the spectrum. The entire EEL spectrum in logarithm scale is shown in the inset.

4. Conclusions

In this work a range of experimental STEM-EELS set-ups has been systematically explored in order to determine the onset of the optical, direct bandgap of high refractive index GaAs-based materials. Acceleration voltages in the range 80 – 120 kV were combined with a broad range of various semi-convergence and -collection angles, on- and off-axis conditions, aloof scanning, and variable TEM specimen thicknesses.

In normal STEM mode and independent of on- or off-axis conditions, specimen thickness and acceleration voltage, the EEL signal in the loss region of the bandgap was totally dominated by contributions from relativistic losses, phonons and excitons, surface losses and guided light modes. The combined signal from these unwanted losses masked the relatively weak signal from bandgap excitations. Furthermore, no background procedure was able to deconvolute the buried bandgap signal from the complex background.

However, we exploited that all relativistic losses and guided light modes are confined inside a narrow forward-scattered solid angle, extending out to a few tens of μrad only. In Low-Mag STEM mode the semi-convergence and –collection angles can both go far down into the μrad range. Such low semi-angles were combined with off-axis conditions to collect electrons scattered to outside the angular range of relativistic losses and guided light modes. Off-axis conditions further suppressed the ZLP and the tail of the ZLP, which allowed the bandgap to be directly seen and extracted from background subtracted spectra. Off-axis conditions mean that we collect electrons that have received a momentum transfer. However, since the off-axis scattering angles that contribute to the EEL signal are small compared to the distance to any Brillouin zone boundary, the detected bandgap excitations are also expected to be equal or close to equal to the material's direct bandgap. These assumptions were confirmed by measured bandgaps that were all (close to) identical to the known or expected direct bandgaps of the GaAs-based materials.

Acknowledgements

The authors would like to thank Professor Shu Min Wang and Mahdad Sadeghi at the Nanofabrication Laboratory at Chalmers University, Sweden for providing the samples. The Norwegian Research Council is acknowledged for funding the HighQ-IB project under contract no. 10415201. The research leading to these results has received funding from the European Union Seventh Framework Programme under Grant Agreement 312483 - ESTEEM2 (Integrated Infrastructure Initiative–I3) through the system of transnational access. R.E. and J.V. acknowledge funding from GOA project "Solarpaint" of the University of Antwerp.

References

1. M. Horak, M. Stöger-Pollach, The Cerenkov limit of Si, GaAs and GaP in electron energy loss spectrometry, Ultramicroscopy 157 (2015) 73-78.
2. R.H. Ritchie, Plasma Losses by Fast Electrons in Thin Films, Phys. Rev 106 (1957) 874-881.
3. R. Erni and N.D. Browning, Valence electron energy-loss spectroscopy in monochromated scanning transmission electron microscopy, Ultramicroscopy 104 (2005) 176-192.
4. P.A. Cerenkov, Dokl. Akad. Nauk, Visible Emission of Clean Liquids by Action of γ Radiation , SSSR 2 (1934) 451.
5. E. Kröger, Calculations of the energy losses of fast electrons in thin foils with retardation, Z. Phys. 216 (1968) 115-135.
6. R. Erni, N.D. Browning, The impact of surface and retardation losses on valence electron energy-loss spectroscopy, Ultramicroscopy 108 (2008) 84-99.
7. E.D. Palik, Handbook of Optical Constants of Solids (1991)1985-1991.
8. L. Gu, *et al*., Band-gap measurements of direct and indirect semiconductors using monochromated electrons, Phys. Rev. B 75 (2007) 195214.
9. M. Stöger-Pollach, H. Franco, P. Schattschneider, S. Lazar, B. Schaffer, W. Grogger, H.W. Zandbergen, Cerenkov losses: A limit for bandgap determination and Kramers–Kronig analysis, Micron 37 (2006) 396-402.
10. R. Erni, On the validity of the Cerenkov limit as a criterion for precise band gap measurements by VEELS, Ultramicroscopy 160 (2016) 80-83.
11. M. Stöger-Pollach, Optical properties and bandgaps from low loss EELS: pitfalls and solutions, Micron 39 (2008) 1092-1110.
12. A.D. Dorneich, R.H. French, H. Müllejans, S. Loughlin, M. Rühle, Quantitative analysis of valence electron energy-loss spectra of aluminium nitride, J. Microsc. 191 (1998) 286.
13. K. van Benthem, C. Elsässer, R.H. French, Bulk electronic structure of SrTiO3: Experiment and theory, J. Appl. Phys. 90 (2001) 6156.
14. S. Lazar, G. Botton, M.-Y. Wu, F. Tichelaar, H. Zandbergen, Materials science applications of HREELS in near edge structure analysis and low-energy loss spectroscopy, Ultramicroscopy 96 (2003) 535.
15. M. Stöger-Pollach, P. Schattschneider, The influence of relativistic energy losses on bandgap determination using valence EELS, Ultramicroscopy 107 (2007) 1178-1185.
16. Arenal, R. and Stephan, O. and Kociak, M. and Taverna, D. and Loiseau, A. and Colliex, C., Electron Energy Loss Spectroscopy Measurement of the Optical Gaps on Individual Boron Nitride Single-Walled and Multiwalled Nanotubes, Phys. Rev. Lett. 95 (2005) 127601.
17. El Allali, M. and Sorensen, C. B. and Veje, E. and Tidemand-Petersson, P., Experimental determination of the GaAs and $Ga_{1-x}Al_xAs$ band-gap energy dependence on temperature and aluminum mole fraction in the direct band-gap region, Phys. Rev. B 48 (1993) 4398-4404.

18. Shan, W. and Yu, K. M. and Walukiewicz, W. and Ager, J. W. and Haller, E. E. and Ridgway, M. C., Reduction of band-gap energy in GaNAs and AlGaNAs synthesized by N implantation, Applied Physics Letters 75 (1999) 1410-1412.
19. Kolhatkar, Gitanjali and Boucherif, Abderraouf and Valdivia, Christopher E. and Wallace, Steven G. and Fafard, Simon and Aimez, Vincent and Arès, Richard, Growth optimization and optical properties of AlGaNAs alloys, Journal of Applied Physics 115 (2014) 163513.
20. B. Rafferty, L. M. Brown, Direct and indirect transitions in the region of the band gap using electron-energy-loss spectroscopy, Phys. Rev. B 58 (1998) 10326--10337.
21. B. W. Reed, M. Sarikaya, Electronic properties of carbon nanotubes by transmission electron energy-loss spectroscopy, Phys. Rev. B 64 (2001) 195404.
22. M.G. Walls, A. Howie, Dielectric theory of localised valence energy loss spectroscopy, Ultramicroscopy 28 (1989) 40 – 42.
23. P. Crozier, T. Aoki, Q. Liu, L. Zhang, Detection and Characterization of OH Vibrational Modes using High Energy Resolution EELS, Microscopy and Microanalysis 21(s3) (2015) 1473-1474. doi:10.1017/S1431927615008144.
24. J.M. Zuo and J.C. Mabon, Web-based Electron Microscopy Application Software: Web-EMAPS, Microsc Microanal 10(Suppl 2), 2004; URL: http://emaps.mrl.uiuc.edu/